Three-Fluid Magneto-Hydrodynamical Simulation of Plasma Focus Discharges

K. Behler, H. Bruhns

IPP 1/244 August 1987

MAX-PLANCK-INSTITUT FÜR PLASMAPHYSIK
8046 GARCHING BEI MÜNCHEN

MAX-PLANCK-INSTITUT FÜR PLASMAPHYSIK

GARCHING BEI MÜNCHEN

Three-Fluid Magneto-Hydrodynamical Simulation of Plasma Focus Discharges

K. Behler, H. Bruhns

IPP 1/244 August 1987

THREE-FLUID MAGNETO-HYDRO-DYNAMICAL SIMULATION OF PLASMA FOCUS DISCHARGES[a]

K. Behler, H. Bruhns

Max-Planck-Institut für Plasmaphysik
Boltzmannstraße 2
D-8046 Garching
Germany

Abstract

A two-dimensional, three-fluid code based on the two-fluid Potter code was developed for simulating the plasma focus discharge. With this code it is possible to treat the neutral gas in addition to the plasma components and to model the ionization and recombination phenomena. Thus one can study the sheet dynamics in a plasma focus and investigate effects such as the occurrence of residual gas (or plasma) density behind the current sheet in the run-down phase. This is a prerequisite to the occurrence of leak currents, which are one of the causes limiting the performance of large plasma focus devices. It is shown that fast operating foci with small dimensions behave favourably compared with the 'classical' Mather focus with long coaxial electrodes.

---

[a] work performed while the authors were affiliated to the Institut für Angewandte Physik II, Universität Heidelberg

I. Introduction

During the past two decades the plasma focus has been studied in a large number of experiments with stored energies ranging from 1 to 1000 kJ /1,2/. The record neutron yields and the scaling of fusion reactions with the square of the energy being fed into the gun nourished expectations of utilizing the plasma focus scheme for developing a (materials-testing) neutron generator. Even a comparatively simple prospective fusion reactor has been under consideration.

However, it soon became obvious that only a minor fraction of nuclear reactions was due to a thermal plasma, the majority being connected with non-Maxwellian, accelerated deuterons. Furthermore, at present there is no fully developed model which would account for the scaling found empirically. Even more problematic is the observation that with increasing size and energy input of the device the scaling deteriorates. One simple reason is that an increasingly larger fraction of the total current no longer flows through the pinch region but links the center and outer electrode elsewhere, particularly in the vicinity of the insulator. Thus the largest experiment, the Frascati plasma focus, was sucessfully operated with only up to one-third of the total energy (320 kJ instead of 1000 kJ); above this value the neutron yield increased only marginally with energy /2/. As a consequence, the scaling was reformulated as the neutron yield proportional to the fourth power of the current flowing through the pinch region.

Interferometric and spectroscopic measurements near the insulator and in the run-down region show residual plasma densities that amount up to 30% of the initial filling density after the plasma sheet has left these regions /3/. It was inferred that the sheet does not fully ionize the gas during the initial stages of the discharge.

It is therefore of considerable importance to investigate the initial stage and the run-down phase of a plasma focus in more detail. Experimental studies are needed. As far as spectroscopy and interferometry are concerned, however, these cannot be unambiguously interpreted since line integration and restricted access impose limitations. Probe measurements in these high-current-density plasmas are also difficult and unreliable.

Numerically, up to now the most elaborated published work reports on two-dimensional two-fluid calculations. These codes do not allow simulation of the ionization dynamics and hence the sheet performance. Presumably, the code most widely in use is the Potter code /4/, which, in its original fashion and in the versions used by Trunk /5/, Vezin /6/ and ourselves /7/, assumes a fully ionized plasma as initial condition in front of the current sheet. Behind the sheet a residual density is artificially set for numerical reasons. A gas lag through the sheet cannot be handled by this code. Other two-dimensional two-fluid MHD calculations are reported by Dyashenko and Imshennik /8/. Their code contains kinetic features to compute jet generation and neutron yield during the pinch phase. Three-fluid calculations for the z-pinch geometry were made in one dimension by Bazdenkov and Vikhrev /9/. These calculations presented evidence that the ionization process during ingnition has a strong influence on plasma sheet formation. A simple calculation was presented by Eltgroth /10/, assuming heuristically the presence of a leak current, which is then matched in amplitude to fit the experimental observations in the Frascati and Livermore machines /10/. A two-dimensional code with treatment of the ionization phenomena is mentioned by Eltgroth /11/, but details and results are not available to us. Another code was written by Maxon and Eddleman /12/, which, from the physics involved, is similar to the Potter code. Nevertheless, these authors note a marked difference in the run-down velocity of the current sheet between their and Potter's code , claiming that Potter did not calculate the proper speed which would be analytically expected from the balance of magnetic pressure and kinetic energy in the sheet. However, this difference is not present in the version of Potter's code which has been available to Vezin, Trunk and to us. (In addition, the difference mentioned is just $2^{1/2}$, a factor which might come in if the filling density were specified in terms of D_2 rather than deuterium atoms.)

In order to address the questions of the sheet dynamics and leak currents, we developed a two-dimensional three-fluid code, the third fluid representing the neutral gas. This code is an extension of the Potter code but includes full ionization dynamics according to the model presented by Duston and Duderstadt /13/. We did not allow for the details of molecular physics, assuming the gas in front of the current sheet to be already dissociated (e.g. by radiative excitation), but we took dissociation into account by averaging the ionization coefficient over atomic and molecular species. With this model it is possible to simulate the main features of sheet development, gas slip through the sheet, and secondary current channels behind the main current path. We feel that the dominant limitation is now imposed by the resolution of the computational mesh rather than by the physics implemented. Another serious restriction may be seen in the assumption of azimuthal symmetry imposed by the two-dimensional model. Thus, filamentations of the sheet, which have been reported by a number of authors as originating early in the discharge and persisting until the plasma pinches, cannot be described. We would like to mention, however, that predominantly the low-energy, low-pressure devices (e.g. optimized for electron and ion beam emission) show strong filamentation, but not the large devices studied in this paper. These machines suffer more from leak currents, and their long, narrow electrode geometry is apt to bury sizeable amounts of residual gas behind the sheet.

An interesting novelty is the development of very fast high-voltage plasma foci. The SPEED experiments by Decker et al. [14,15] are pioneering in this direction. We studied these experiments in our simulations and found attractive features compared with the standard, medium-voltage Mather experiments.

The following section provides a description of the physical model implemented in our code. Section III then presents the simulations for the fast SPEED experiments. Section IV deals with the behaviour of the main-line experiments at Frascati [2] and Stuttgart (POSEIDON) [16], and finally, in Section V, a discussion concludes our investigations.

II. The model

The starting point for the development of our code is the two-fluid Potter code [4], which has been used for a decade to support experimental studies at Culham [17], Limeil [18], Stuttgart [16], Frascati [2] and Heidelberg [19]. The magnetohydrodynamic equations in this code are described in detail elsewhere [4, 5, 6, 7]. They are solved for six unknown variables, namely the mass density ϱ, the radial and axial moments ϱv_r and ϱv_z, the ion and electron temperatures T_i and T_e and the azimuthal magnetic field B_φ. All other quantities follow from these variables. The boundary conditions are given by the electromechanical equation for the outer circuit,

$$L_0 \frac{dI}{dt} + \frac{d}{dt}(L_i\, I) = \frac{Q}{C} \quad \text{with} \quad L_i\, I = \int \overline{B} \cdot d\overline{f}\ , \quad Q = C\, U_0 - \int I\, dt \quad , \tag{1}$$

the symmetry relations, and the settings in the mesh to provide physically reasonable conditions at the electrode and insulator surfaces [4]. Transport coefficients are used as given by Spitzer [20] for the case without magnetic field and by Shkarofsky et al. [21] for heat conduction in a magnetic field, and for the stress tensor [4]. For simplicity, the Coulomb logarithm is taken to be independent of temperature and density as $\ln\lambda = 10$. (Presumably, the version of the code which was used by Trunk erroneously used a value of $\ln\lambda = 30$ as fixed standard setting.)

To simulate the neutral gas, a third fluid is introduced. Three-fluid codes have already been developed for other plasma devices /9, 11, 22, 23, 24/. The particular geometry of the plasma focus leads to the introduction of four additional unknown variables, namely the neutral mass density ϱ_0, the radial and axial momenta of the neutral fluid $\varrho_0 v_{r0}$, $\varrho_0 v_{z0}$ and its temperature T_0. Hence we obtain the following system of equations:

$$\frac{\partial \rho}{\partial t} + \nabla \cdot (\rho \overline{v}) = \left.\frac{\delta \rho}{\delta t}\right|_{gen-rec} , \tag{2}$$

$$\frac{\partial \rho_0}{\partial t} + \nabla \cdot (\rho_0 \overline{v}_0) = -\left.\frac{\delta \rho}{\delta t}\right|_{gen-rec} , \tag{3}$$

$$\frac{\partial (\rho \overline{v})}{\partial t} + \nabla \cdot (\rho\, \overline{v}\, \overline{v} + p\, \overline{\overline{1}} + \overline{\overline{\overline{V}}}) - \overline{j} \times \overline{B} = \left.\frac{\delta (\rho \overline{v})}{\delta t}\right|_{coll.\ exch.} + \left.\frac{\delta (\rho \overline{v})}{\delta t}\right|_{charge\ exch.} , \tag{4}$$

$$\frac{\partial (\rho_0 \overline{v}_0)}{\partial t} + \nabla \cdot (\rho_0 \overline{v}_0 \overline{v}_0 + p_0 \overline{\overline{1}} + \overline{\overline{\overline{V}}}_0) = -\left.\frac{\delta (\rho \overline{v})}{\delta t}\right|_{coll.\ exch.} - \left.\frac{\delta (\rho \overline{v})}{\delta t}\right|_{charge\ exch.} , \tag{5}$$

$$\frac{\partial (\rho \epsilon_e)}{\partial t} + p_e \nabla \cdot \overline{v}_e + \nabla \cdot (\rho \epsilon_e \overline{v}_e + \overline{q}_e) = \eta j^2 - Q_{ei} - Q_{rad} - Q_{gen} - Q_{e0} , \tag{6}$$

$$\frac{\partial (\rho \epsilon_i)}{\partial t} + p_i \nabla \cdot \overline{v} + \nabla \cdot (\rho \epsilon_i \overline{v} + \overline{q}_i) + \overline{\overline{\overline{V}}} : \nabla \overline{v} = Q_{ei} - Q_{i0} , \tag{7}$$

$$\frac{\partial (\rho_0 \epsilon_0)}{\partial t} + p_0 \nabla \cdot \overline{v}_0 + \nabla \cdot (\rho_0 \epsilon_0 \overline{v}_0 + \overline{q}_0) + \overline{\overline{\overline{V}}}_0 : \nabla \overline{v}_0 = Q_{i0} + Q_{e0} , \tag{8}$$

$$\epsilon = \frac{T}{\gamma - 1} , \qquad \gamma = \frac{c_p}{c_v} = \frac{5}{3} . \tag{9}$$

Owing to the azimuthal symmetry and the occurrence of only B_φ , div $\overline{B}$ is automatically satisfied and Maxwell's equations reduce to

$$\frac{\partial \overline{B}}{\partial t} = -\nabla \times \overline{E}\ , \qquad \nabla \times \overline{B} = \mu_0 \overline{j}\quad , \tag{10,11}$$

and Ohm's law is

$$\overline{E} = \eta \overline{j} + \frac{m_i}{\rho e}\left(\overline{j} \times \overline{B} - \nabla p_e\right)\quad . \tag{12}$$

Most of these equations are self-explanatory. It should be noted that in the energy equations (6 - 8) the convective and advective terms contain the velocities of the species under consideration.

Apart from the ion density - or ambipolar - plasma density, we thus also need the electron velocity:

$$\overline{v}_e \;=\; \overline{v} \;-\; \frac{m_i\, \overline{j}}{\rho e}\quad . \tag{13}$$

In eq. (6) we included Joule heating, energy exchange with ions and neutrals, losses by bremsstrahlung and ionization. Equations (7,8) contain the exchange between ions and neutrals as well as with electrons. Additionally, heating by physical viscosity of the individual constituents, energy changes by generation, recombination, charge exchange and elastic collisions between the species are considered.

While the above equations are solved in a two-dimensional mesh by applying the Lax-Wendroff scheme, we have to solve additional equations for the local energy balance. Concerning the energy transfer between the species by elastic processes, we use the rates

$$Q_{ei_{eq}} = \frac{3}{2}\,\rho\,\frac{T_e - T_i}{\tau_{eq}} \quad , \quad Q_{e0_{eq}} = \frac{3}{2}\,\rho\,\frac{T_e - T_0}{\tau_{eq_{e0}}} \quad , \quad Q_{i0_{eq}} = \frac{3}{2}\,\rho\,\frac{T_i - T_0}{\tau_{eq_{i0}}} \quad , \tag{14}$$

where the relaxation times are given by the classical expressions /21, 22, 23, 25/

$$\tau_{eq} = \frac{1}{2\nu_{ei}}\,\frac{m_i}{m_e} \quad , \quad \tau_{eq_{e0}} = \frac{3}{8}\,\frac{m_0}{m_e}\,{}^{1}\!/\nu_{e0} \quad , \quad \tau_{eq_{i0}} = \frac{3}{8}\quad {}^{4}\!/\nu_{i0} \quad , \tag{15}$$

and the radiation losses by bremsstrahlung

$$Q_{rad} = 1.69 \cdot 10^{-32}\,\rho^2\,T_e^{\frac{1}{2}} \quad \text{watt cm}^{-3} \quad . \tag{16}$$

The energy expended for ionization of the neutral gas is drawn from the electron energy

$$Q_{gen} = \frac{3}{2}\,\frac{\delta\rho}{\delta t}\bigg|_{gen}\chi \quad , \quad \text{with} \quad \chi = 13.6 \text{ eV} \quad . \tag{17}$$

The exchange of energy between the species corresponds to equipartition and includes contributions from the generation-recombination and charge exchange processes

$$Q_{ei} = Q_{ei_{eq}} \quad , \quad Q_{e0} = Q_{e0_{eq}} \quad , \quad Q_{i0} = Q_{i0_{eq}} + Q_{i0_{gen-rec}} + Q_{i0_{charge\ exch.}} \quad , \tag{18}$$

$$\begin{aligned} Q_{i0_{gen-rec}} &= \frac{3}{2}\left(\frac{\delta\rho}{\delta t}\bigg|_{gen} - \frac{\delta\rho}{\delta t}\bigg|_{rec}\right)(T_i - T_0) \quad , \\ Q_{i0_{charge\ exch.}} &= \frac{3}{2}\,\frac{\delta\rho}{\delta t}\bigg|_{charge\ exch.}(T_i - T_0) \ , \text{with} \ \frac{d\rho}{dt}\bigg|_{charge\ exch.} = \xi_{Ex}\,\rho\,\rho_0 \quad . \end{aligned} \tag{19}$$

The momentum transfer between neutrals and electrons can be considered via a modified collision frequency in the expression for the conductivity, while between ions and neutrals the exchange is given by

$$\left(\frac{\delta\rho v}{\delta t}\right)_{coll.\ exch.} = \frac{\rho}{2}\,(v_i - v_0)\,\nu_{i0} \quad , \quad \frac{\delta\rho v}{\delta t}\bigg|_{charge\ exch.} = \frac{\delta\rho}{\delta t}\bigg|_{charge\ exch.}(v_i - v_0) \quad . \tag{20}$$

A different treatment is necessary for the inelastic processes. In general, a wide variety of effects might be taken into consideration. However, we restrict ourselves to the most important ones and hence neglect molecular physics as well as atomic excitations. Explicitly, we only consider electron impact ionization from the ground state, radiative recombination, three-body Auger recombination, and charge exchange. Other processes might be included in a rough approximation by adjusting the coefficients of these terms. This seems to be the only possibility if the introduction of more than one neutral fluid is to be avoided.

The treatment chosen is based upon the findings of Duston and Duderstadt /13/, who show that equilibrium models are inappropriate for the description of ionization and recombination in dense plasmas where high current densities lead to a rapid change of the electron temperature. Instead, they demonstrate that a reduced version (accounting only for the ground states) of the collisional-radiative model of Bates et al. /26/ leads to a physically reasonable and numerically affordable description of inelastic processes. We use the following rate coefficients (valid for hydrogen or deuterium only /13/):

$$\alpha = 5.2 \cdot 10^{-14} \left(\frac{\chi}{T_e}\right)^{\frac{1}{2}} \left[0.43 + \frac{1}{2} \ln \frac{\chi}{T_e} + 0.47 \left(\frac{\chi}{T_e}\right)^{-\frac{1}{3}}\right] \quad \mathrm{cm}^3\,\mathrm{s}^{-1} \quad , \tag{21}$$

$$\beta = 8.051 \cdot 10^{-28} \frac{1}{\chi^2 T_e} \quad \mathrm{cm}^6\,\mathrm{s}^{-1} \tag{22}$$

for radiative and Auger recombination, respectively. The ionization rate coefficient is written in an expansion /27/

$$\ln < \sigma v >= \sum_{i=0}^{n} A_i (\ln T_e)^i \quad . \tag{23}$$

The expansion coefficients are given in Table I.

Since ionization and recombination are extremely strong functions of electron temperature and density, respectively, it is not possible to solve the resulting equation

$$\frac{dn}{dt} =< \sigma v > n\, n_0 - \alpha\, n^2 - \beta\, n^3 \tag{24}$$

within the algorithm for the MHD equations because numerical stability would require unacceptably small time steps. Instead, we use a predictor-corrector scheme which iteratively computes the local rate coefficients when and wherever a change in electron temperature of more than 10% occurs. Equation (24) is then solved in a separate, implicit procedure /28/, while the main MHD calculation uses an explicit algorithm.

As the calculations show, radiative recombination contributes little to the local power balance; convective transport and impact ionization dominate. Line radiation from hydrogen can only play a role behind the sheet but is neglected. Radiation from impurities is important only close to solid surfaces at normal focus operation and can be thought to be included by the boundary condition of fixed temperature (see below).

Special handling is required for regions of low density which occur behind the current sheet. In the two-fluid versions of the code, a pedestal (or fixed minimum density) was used. Below this value the MHD computation was replaced by the vacuum solution of Maxwell's equations. A procedure like this is necessary since the Alfvén speed becomes large in low-density regions and consequently numerical stability criteria, e.g. of the kind $\Delta t \ll \Delta x/v_{max}$, are violated.

Although we cannot completely avoid such a cut-off, we try to use a more appropriate scheme by taking the Alfvén speed directly, rather than the density, as a criterion. Thus the temporal and spatial extents of the cut-off region are drastically reduced. We also have to impose a minimum for the neutral density below which the computation of the neutral variables is halted. Table II gives the variables and their settings below the two thresholds.

There are other boundary conditions of geometrical nature. Especially, we treat all electrode and insulator surfaces as impermeable with the exception of the tip of the center electrode since usually hollow electrodes are used experimentally. Temperatures are held fixed at 2 eV on the surfaces. Velocities normal to solid surfaces are pulled down to zero in the boundary mesh elements. These conditions are also used in the two-fluid versions of the code.

III. The SPEED experiments

The SPEED experiments by Decker and co-workers are designed to optimize the matching of the external circuitry with the coaxial accelerator by selecting a more appropriate voltage /14, 15/. Hence SPEED 1 has a design voltage of 200 kV with energy storage of 30 kJ, while the new SPEED 2 can run up to 300 kV with 187 kJ. Owing to the high voltage the period of the LC circuit is comparatively short for both devices (1.6 µs), and so the accelerator is also very short in length (4.5 and 3.5 cm, respectively).

A. SPEED 1

We start the 3-fluid calculation with a 10% homogeneously ionized deuterium plasma. The temperature is assumed to be 2 eV for all components, corresponding approximately to the ionization equilibrium. For comparison we run the 2-fluid code (full ionization) at the same base temperature.

The initial current through the device is chosen as 1 kA. This current is necessary ab initio for computational reasons and is assumed to flow along the insulator. Subsequently, the total current is determined by the equation of the external circuit, eq. (1).

To attain a very good resolution (0.8 mm radially, 1.2 mm axially), we restrict the mesh to a rectangle of 1 by 5 cm next to the bottom of the gun, bounded radially inwards by the insulator. Axially, the area of computation extends 1.5 cm beyond the insulator. We can thus observe the initial stage of the discharge; however, after 120 ns the sheet reaches the border of the computational frame and we have to stop the calculation and resort to a coarse mesh. To discuss the events, we use a fixed point of observation, r = 2.6 cm, z = 1.6 cm, which is axially approximately in the middle of the insulator and radially 0.16 cm above it, i.e. two mesh points away from it (Fig. 1). Initially, little spatial dynamics is found in the plasma sheet. The temporal profiles at the fixed point of observation therefore give reasonable insight into the development of the sheet. Since, in the first 10 - 20 ns the plasma density is low, the electron temperature rapidly attains a value of about 4 eV when impact ionization in the electric field sets in (Fig. 2). Now a decrease of neutral density and a corresponding increase of plasma density starts for the next 50 ns, while the temperature stays at 4 eV, the ohmic heating being balanced by ionization. Depending on the current level and the time constant of the external circuit, the value of T_e varies between 2.5 eV and 4.5 eV (SPEED 1 at maximum charging). When more than 50% of the particles are ionized, T_e starts to increase slightly.

At 75 ns after 'breakdown' the sheet begins to lift off from the insulator, i.e. at the fixed point of observation we see a decrease in plasma density. After 130 ns a residual neutral density around 10 to 15 % of the fill remains in a layer about 2 - 3 mm thick around the insulator, the plasma density being below 10%. Then, the normal computation stops (at the particular point of the mesh) and the vacuum solution is implemented. This procedure leads to some oscillations in the calculated values of T_e.

Investigating the spatial behaviour at different times (Fig. 1), we see that the sheet lifts off almost perfectly like an inverse pinch. At the (axial) front end, where the current leaves the electrode, the ionization is strongest, good conduction of the plasma is generated and very steep magnetic field gradients are obtained. Here the sheet is thinner than in the radially moving part of the plasma, the computed thickness being limited by the mesh size.

We now turn to the standard mesh size with axial and radial cell dimensions of 2.6 mm and 3.8 mm, respectively, at a time when the sheet has moved radially about 1.8 cm (250 ns, Fig. 3). Note the density left behind the sheet near the insulator in Fig. 3a. The ionization at the current level in the first 200 ns of the discharge is not complete, the electron and ion temperatures reach maximum values of about 16 and 6.5 eV, respectively, at the rear end of the sheet. The plasma density has almost equal gradients at the front and rear. This is quite different from the two-fluid code, where there is a steep gradient behind the sheet but a weak one in front of it (in Fig. 3c all contours except the most outward belong to the rear side and hence show a radially increasing density). The temperatures are similar in the two codes only in regions of almost complete ionization. Otherwise the three-fluid calculation gives lower values.

At this time (250 ns) the behaviour at the tip of the current sheet in the three-fluid model has inverted: the area of current contact to the electrode is large, the temperatures lower and, ionization is incomplete, the sheet moves faster axially than in the two-fluid runs. Hence the sheet has moved 5 mm further in the three-fluid model than in the two-fluid one. (There is no difference between fine and coarse mesh calculations.)

Globally, one can describe the first 50 ns as the main ionization phase. Up to 150 ns the sheet build-up is significant; later on there are no pronounced changes in the (relative) gradients, hence the plasma is in the run-down phase. This is consistent with experimental observations /15/. However, in the case of large, slow machines there is no pronounced distinction between the run-down and compression phases. We see that at 250 ns the sheet has almost reached the front end of the center electrode. The axial velocity is about 20 cm/µs, about 8% faster than in the two-fluid code. Also during this time a neutral density of up to $2 \cdot 10^{16}$ cm^{-3} is left behind, the maximum being close to the center electrode (at z = 4-6 cm).

Beyond the tip of the center electrode the accelerated sheet continues to move axially. The gas in front of the electrode now constitutes the reservoir for the build-up of a radially moving sheet. The radial velocity attained is $1.25 \cdot 10^7$ cm/s, the radial pinch proceeds in 250 ns leading to a total time of 510 ns from breakdown to maximum compression. Experimentally, for the set of parameters which we use in the calculations Decker et al. find a somewhat faster pinch, the maximum compression occurring at 470 ns.

We think this deviation is reasonable, if we take into account that the calculation is somewhat more restrictive in the ionization than will happen experimentally since no radiative ionization in front of the sheet is implemented and also the shock characteristics are not sufficiently treated in the code. Hence the dynamics in the experiment might be somewhat faster. We see no reason, however, for calculating the sheet thickness much too large. Experimentally one observes a sheet thickness of below 1 mm (inferred from schlieren and shadow measurements [29]). Although a problem in itself, this discrepancy should not influence the comparison of the sheet dynamics unless we invoke kinetic effects for ionization, which may strongly depend on scale lengths (e.g. gyromotions of particles in the sheet /15/).

With respect to the global circuit features there exists good agreement between the calculations and the experimental results. Decker and co-workers/15/ show in their fig. 8 the total current and power versus time. The maximum current of 770 kA appears at 370 ns. In the calculation we find 780 kA at 380 ns - the time when the inductance increases owing to the axial compression in front of the center electrode. Up to this time, the inductance in both the code and the experiment shows a similar behaviour: first a steep increase with the current path build-up, then a flatter slope during ionization of neutrals and sheet formation. When the sheet lifts off from the insulator, radial expansion (inverse pinch) in combination with axial acceleration makes the inductance grow faster than before during sheet formation. During the now beginning run-down phase the inductance increases linearly since the axial velocity of the sheet becomes constant and radial expansion slows down. However, during the pinch phase the decrease of total current is less pronounced in the computations than observed experimentally. This corresponds to the fact that the pinch radius remains much larger in the calculation than inferred from schlieren pictures. The late pinch phase can then no longer be simulated correctly since apart from problems due to the finite mesh size the MHD-model breaks down.

B. SPEED 2

The main computations for the new SPEED 2 device/30/ were performed during the scaling considerations for the experiments. We find breakdown and sheet formation which are only marginally slower than with SPEED 1, where the current build-up is slightly faster. As a consequence, however, after 200 ns a 5 mm thick, fully ionized sheet has been established 1 cm in front of the insulator, this being thicker than in SPEED 1. These results are obtained with the estimated operational maximum density of 6 mbar (other parameters are given in Table III). Then the maximum compression is calculated at t = 700 ns, approximately 200 ns too late compared with the cycle time of the current. This can be corrected by reducing the diameter of the inner electrode and/or the fill density. We mention that also in the case of SPEED 1 semiempirical analytical scaling of the electric circuit and the (rigid) plasma dynamics tends to overestimate the plasma motion.

IV. The large experiments

A. The FRASCATI experiment

The Frascati plasma focus is the largest experiment which has been operated so far. With an installed energy of 1 MJ the expectations for fusion neutron yields ranged into the 10^{13} regime [2].

As already mentioned, however, these values have never been reached, the deviation from the I^4 scaling law being attributed mainly to the leakage currents behind the main current sheet.

Here we want to focus on a particular set of machine parameters at W_0 = 250 kJ which was studied experimentally in great detail. This is true especially with respect to the measurement of the current density and residual plasma density in the vicinity of the insulator [3]. Figure 4 shows the calculated temporal profiles of the plasma and neutral densities and the electron temperature at a fixed observation point close to the insulator. As with the SPEED calculations, we start with 10% ionization and an initial equilibrium temperature of 2 eV.

In the first phase of the discharge we calculate a rise in the electron temperature which levels off at 2.5 eV, being balanced by the drain due to ionization. This temperature is lower than in the SPEED experiments since the slow external circuit provides much less specific ohmic heating. Again, the temperature remains approximately constant until the product of neutral and plasma density decreases. It is interesting that in this device the plasma density reaches only 30% of the initial filling density at the instant of sheet lift-off from the insulator (t = 800 - 900 ns) while the neutral density decreases to 50%. At t = 1 µs the sheet has left the reference point. From then the neutral density continuously decreases, while a residual plasma density of almost 25 to 30% of the fill remains behind the sheet. The ionization level is maintained at an electron temperature of 2 - 3 eV; the energy is provided by a finite current density which continues to flow there. The situation is found to be similar all over the insulator region.

During the run-down phase (t = 1 - 5.8 µs) the plasma sheet becomes dense and the temperatures increase considerably. The current density now provides so much heating power that the neutral gas which is collected by the sheet is ionized right in front of the shock, and no significant difference is found in the temperatures compared with two-fluid calculations. However, near the walls the plasma stays cooler (we maintain as a boundary condition a constant temperature of

2 eV at the electrode surface). Thus ionization proceeds more slowly here and neutral gas can slip through the sheet, providing partially ionized gas behind it which gradually fills the whole interelectrode gap.

In contrast to the two-fluid model, which has to assume full ionization, the calculations thus clearly show the two main disadvantages of the large plasma focus machines at standard charging voltage (40 - 80 kV): the matching of the external circuit to the gun requires large electrodes whose surfaces allow gas to creep behind the sheet and the current rises too slowly for complete initial ionization.

During the final radial compression in front of the coaxial gun the electron temperature of the plasma in the vicinity of the insulator suddenly rises to more than 10 eV and the degree of ionization in this region increases to almost 100%. The increase of total inductance in the gun (Fig. 4) corresponds to a loop voltage of about 20 - 40 kV, which leads to a decrease of the current from 3 to 1.3 MA. However, it is unlikely that only the external circuit responds to this change of inductance, rather we may expect current loops to be generated by the EMF across the coaxial gun, which might partially decouple the pinching plasma sheet from the external source. This phenomenon has been observed experimentally /3/ and, similarly, we find current loops in the vicinity of the insulator. However, we are not sure whether the magnitudes of both the area and current are more strongly influenced by the numerical procedure (in these regions the very large Alfvén speed forces us to use a vacuum solution over part of the computational mesh area) or by physical issues. This question is left open here since much more detailed investigation would be required.

B. The POSEIDON experiment

It is worth while to compare the simulation of the Frascati machine with POSEIDON, the 500 kJ experiment at Stuttgart/16/. Here similar difficulties are encountered experimentally. We therefore present calculations for operation at 280 kJ, which has been an experimental standard setting for some time. Owing to the difference in external inductance and charging voltage the initial dI/dt is four times faster in POSEIDON than in the Frascati machine. Unfortunately, we are not aware of any measurements of the plasma behaviour in the insulator region at the ignition time. We have, however, some control of our simulation by the experimental observations of the dynamics in the run-down phase, which compare well with the calculations.

In Fig. 5 we present results for POSEIDON similar to those in Fig. 4 . While the absolute time scales are different in the two machines, the ionization progress turns out to be comparable. We see that initially POSEIDON performs better and a higher fraction of the neutral filling gas is ionized before the sheet lifts off. Nevertheless, the fraction of unaccelerated gas in front of the insulator is not negligible (Fig. 6). At t = 400 ns this partially ionized plasma carries a leakage current of about the same magnitude as the current flowing in the main sheet (which, however, still continues to increase). This leakage current is present in the calculation until numerical stability requirements force us to set vacuum conditions at about t = 800 ns.

In the run-down phase (0.4 μs ‹ t ‹ 2 μs, i.e. after the inverse pinch has reached the outer electrode) the behaviour found in the calculations is similar to that in the Frascati machine. One-third of the fill is left behind the sheet owing to the incomplete ionization close to the electrodes; in the center of the interelectrode gap we find a gas slip of 10%.

Near the outer electrode a strong accumulation of the gas is observed, leading to a long, dense tail of the sheet which in the calculation cannot be ejected from the run-down channel but fills the interelectrode gap. As an average, a density of a few times 10^{16} cm^{-3} remains between the electrodes, originally being in the plasma state but rapidly cooling off and partially recombining during the time of interest. Experimentally, different types of outer electrodes were used; in the calculations we refer to the case of an almost closed electrode [31] consisting of narrow-spaced bars. (This is the most natural one to simulate.) It is evident, however, that an outer electrode which is partially transparent to the gas would be favourable in the present context. An improvement might be obtained if such an electrode were combined with fast gas-puff operation into the interelectrode space. There are, however, other considerations such as avoiding filamentation or reducing the current density at the electrode surfaces, which may conflict with a transparent outer electrode in an experiment.

Note that the tail formation at the outer electrode is much more pronounced in the case of POSEIDON than in the simulation of the Frascati experiment because the rather thin center electrode (r_{ie} = 6.65 cm as compared with 18.5 cm in Frascati) leads to a stronger radial curvature of the current sheet, which favours gas slip along the periphery. (Only after the sheet has axially moved beyond the center electrode does the curvature invert and approach the form found in the simulation of the Frascati experiment.)

At the time of maximum current (1.5 µs, 2.7 MA) the run down phase is not yet completed. It takes another 1.1 µs until the pinch occurs in front of the center electrode. Nevertheless, the code shows a maximum density of $1 \cdot 10^{19}$ cm^{-3} at an electron temperature of approximately 1 keV. There are indications of a m = 0 structure in the numerical results. Since, however, the wavelength correlates with the mesh steps, we assume computational origins and do not believe that it has any physical relevance. Furthermore, numerical instabilities in the evaluation of the electron temperature force us to stop the calculations at this point.

V. Conclusion

We have shown that the implementation of a third, neutral fluid into a two-dimensional MHD code provides a considerably more detailed account of the dynamics of plasma focus machines during the inverse pinch and run-down phases.

In particular, we find in the computations serious residual gas and plasma densities behind the current sheet. This is consistent with the experimental observation of leakage currents during the pinch phase (i.e. during the steep increase of inductance in the main sheet) which have the same magnitude as the current in front of the coaxial structure. This is one reason why the performance of plasma foci does not match simple electromechanical scaling laws.

There is also clearly demonstrated, however, that fast current build-up is favourable to prevent residual densities back in the gun. For instance, the POSEIDON experiment at Stuttgart initially shows much better behaviour in this respect than the slower Frascati machine.

A problem remains in the fact that long, thin electrode structures (needed to match low-voltage external energy storage) are disadvantageous for completely purging the interelectrode space of residual gas. This seems to cause major current leakage. An electrode geometry with larger radii than were investigated in the Frascati experiment and also at Stuttgart (we do not present simulations for this case here) may result in a more efficient snow-plough.

Comparison of the large, low-voltage devices with the fast SPEED experiments makes the very good performance of these machines apparent. Establishment of a sheet proceeds much faster and an electron temperature a factor of almost two higher is already attained during the inverse pinch. This leads to much lower residual gas and plasma densities than in the cases discussed in Section IV. We see in this fact an additional benefit from the rationale of these experiments which originated in the optimization of energy commutation into the gun [14].

There is comparatively good agreement in all cases between the calculation of the overall features of the discharges and the experiments. One has, of course, to take into account that the code, irrespective of its actual complexity, simplifies the experimental situation in many respects, and much further work would be required to overcome this. We want to draw attention to two aspects which, in our view, very severely limit the results obtained. First, there is the ad-hoc initialization of the current in the calculation along the insulator surface. For some experimental settings, this seems to be a very appropriate method. (Perhaps the most striking indication is the discussion by Decker et al. [32] concerning the changes in behaviour of plasma foci with different polarity of the electrodes, which demonstrates the importance of currents close to the surface of the insulator for the development of the current sheet and the quality of the final pinch.) We know, however, that a 'diffuse' breakdown also constitutes a possible start for a focus discharge and that for optimum performance (as judged from the neutron emission) the large machines tend to have some intermediate start that is between being adjacent to the insulator and diffuse over the interelectrode gap /2/. Altogether, the initial boundary conditions in our calculation may not be of complete appropriateness and may therefore lead to slight mismatch in the dynamics of the plasma as compared with experimental results.

We have tried to investigate the influence of a diffuse breakdown by forcing 50% of the initial current to flow close to the insulator surface, the rest being smoothly distributed over the interelectrode gap along the whole insulator length. However, as may be expected if one considers the inductance of the different current paths, the 'diffuse' part of the current density is somewhat starved, while the low-inductance rear sheet moves more rapidly and fetches the diffuse front in the early run-down phase. Thus, there is little influence on the later dynamics, nor does the thickness of the sheet change dramatically.

A second restriction on a proper comparison is of course the unavoidably simplified treatment of boundary conditions, which seems to be of much more influence in the three-fluid code than in the two-fluid treatment. This is due to the strong dependence of the ionization dynamics on the temperature and hence on the assumed energy sink in the wall. The settings in our calculation (10% initial ionization and, correspondingly, an electron temperature of 2 eV) stem mainly from computational requirements: the increasing Alfvén time does not allow much less than 10% density to be calculated properly without running into unstable situations: one then has to resort to a 'vacuum treatment' using a fixed pedestal for the density and a decoupled set of dynamic and electromagnetic equations.

We conclude the discussion of imperfections by considering the settings for the outer electrode. Clearly, the assumption that no mass transport to larger radii is possible conflicts with the experimental situation in many machines. However, this restriction does not seem to be serious for the cases discussed here. The large machines have rather closed outer electrodes, mainly because experimental observations show that electrodes with fewer or thinner rods will not improve performance. Two possible reasons have been stated. Fortunately, with the SPEED experiments, the settings for the outside of the computational mesh are irrelevant since the current sheet does not reach this boundary during the time of interest. This is consistent with the experimental situation where the outer electrode is not touched by the current until late after the pinch (but, curiously enough, the (non-)existence of an outer electrode influences the discharge)/30/.

In summary, our calculations give reasonable agreement with the experiments discussed and show the distinct advantage of small, fast plasma focus geometries over the more conventional Mather-type guns.

Acknowledgement

We would like to thank the members of the experimental groups at Düsseldorf, Frascati, Stuttgart and Heidelberg for their stimulating interest in this work. We are indebted to Prof. Dr. K. Hübner for valuable discussions and the institutional support. It is a pleasure to acknowledge the help of Prof. Dr. G. Decker and Dr. W. Kies in making possible the detailed interplay between experimental and computational work for the SPEED devices.

References

1. Mather J. W., **Methods of Experimental Physics**, edited by Griem H. and Lovberg R., Vol. **9B**, p. 187, Academic Press, New York and London (1971);

   Krompholz H., Michel L., Schönbach K.H., Fischer H., Appl. Phys. **13**, 29 (1977);

   Decker G., Herold H., Kaeppeler H.J., Kies W., Maysenhölder W., Nahrath B., Oppenländer T., Pross G., Rückle B., Sauerbrunn A., Schilling P., Schmidt H., Shakhatre M., Trunk M., and Steinmetz K., Bruhns H., Ehrhardt J., Hübner K., Kirchesch P., Mechler G., Plasma Phys. and Contr. Nuclear Fusion Res., Proceedings of the Seventh International Conference, Innsbruck, 1978, (IAEA, Vienna, 1979) Vol. II, p. 135

2. Gourlan C., Kroegler H., Maisonnier Ch., Rager J.P., Robouch B.V., Gentili A., Plasma Phys. and Contr. Nuclear Fusion Res., Proceedings of the Seventh International Conference, Innsbruck, 1978, (IAEA, Vienna, 1979) Vol. II, p. 123

3. Gourlan C., Kroegler H., Maisonnier Ch., Oppenländer T., Rager J.P., Contr. Fusion and Plasma Phys., Proceedings of the Eigth Europ. Conf., Prague, 1977, (Czechoslovak Academy of Sciences, Prague, 1977), Vol. II, 247

4. Roberts K.V., Potter D.E., **Methods in Computational Physics**, edited by Alder et al., Vol. **9**, 340, Academic Press, New York and London (1970);

   Potter D.E., Phys. Fluids **14**, 1911 (1971)

5. Trunk M., Plasma Phys. **17**, 237 (1975)

6. Vezin R., priv communication

7. Behler K., phd thesis, University of Heidelberg (1984)

8. Dyachenko V.P., Imshennik V.S., Sov. Phys. JETP **29**, 947 (1969)

9. Bazdenkov S.V., Vikhrev V.V., Sov. J. Plasma Phys. **1**, 250 (1976)

10. Eltgroth P., Phys. Fluids **25**, 2408 (1982)

11. Eltgroth P., priv. communication

12. Maxon S., Eddleman J., Phys. Fluids **21**, 1856 (1978)

13. Duston D., Duderstadt J., J. Appl. Phys. **49**, 4388 (1978)

14. Decker G., Flemming L., Kaeppeler H.J., Oppenländer T., Pross G., Schilling P., Schmidt H., Shakhatre M., Trunk M., Plasma Phys. **22**, 245 (1980)

15. Decker G., Kies W., Pross G., Phys. Fluids **26**, 571 (1983)

16. Herold H., Bertalot L., Deutsch R., Grauf W., Jäger U., Kaeppeler H.J., Lepper F., Oppenländer T., Schmidt H., Schwarz J., Schwörer K., Shakhatre M., Hayd A., Maurer M., Meinke P., Plasma Phys. and Contr. Nuclear Fusion Res., Proceedings of the Ninth International Conference, Baltimore, 1982, (IAEA, Vienna, 1983) Vol. **II**, p. 405;
Herold H., Bertalot L., Hirano K., Jäger U., Kaeppeler H.J., Sadowski M., Schmidt H., Schmidt R., Shakhatre M., Shyam A., Böckle G., Matl K., Wenzel N., Wolf R., Bätzner R., Hinsch H., Hübner K., Plasma Phys. and Contr. Nuclear Fusion Res., Proceedings of the Tenth International Conference, London, 1984, (IAEA, Vienna, 1985) Vol. **II**, p. 579

17. Forrest M.J., Peacock N.J., Plasma Phys. **16**, 489 (1974)

18. Basque G., Patou C., Vezin R., Proceedings of the Second Topical Conf. on Pulsed High-Beta Plasmas, Garching, 1972, paper E2, (Max-Planck-Institut für Plasmaphysik, Garching, FRG, 1972),

19. Böckle G., priv. communication

20. Spitzer L., **Physics of Fully Ionized Gases**, J. Wiley & Sons, 2nd ed., London (1962)

21. Shkarofsky I.P., Can. J. Phys. **39**, 1619 (1961)

22. Duechs D., Griem H., Phys. Fluids **9**, 1099 (1966)

23. Becker G., Duechs D., Nucl. Fusion **16**, 763 (1975)

24. Sgro A.G., Phys. Fluids **21**, 1410 (1978)

25. Cravath A.M., Phys. Rev. **36**, 248 (1930)

26. Bates D.R., Kingston A.E., McWhirter R.W.P., Proc. R. Soc. London **A267**, 297 (1962)

27. Freeman R.L., Jones E.M., **Atomic Collision Processes in Plasma Physics Experiments: Analytic expressions for selected cross-sections and Maxwellian rate coefficients**, UKAEA CLM-R 137, H. M. Stationery Office*), London (1974); Jones E.M., **Atomic Collision Processes in Plasma Physics Experiments: Analytic expressions for selected cross-sections and Maxwellian rate coefficients II**, UKAEA CLM-R 175, H. M. Stationery Office*), London (1977)

*) government publication available from: Her Majesty's Stationery Office, Government Bookshop, 49 High Holborn, London WC 1V6HB

28. Richtmyer R.D., Morton K.W., **Difference Methods for Initial-Value Problems**, Interscience, 2nd ed., New York (1967)

29. Decker G., Kies W., Pross G., Rybach J., Proceedings of the 3rd Int. Workshop on Plasma Focus Research, Stuttgart, 1983, (Institut für Plasma Forschung, Stuttgart, 1983), p. 75

30. Decker G., priv. communication

31. Schmidt H., priv. communication

32. Decker G., Kies W., Pross G., Phys. Letters A, **89**, 393 (1982)

Tables

	$< \sigma v >$	ξ_{Ex}
A_0	$-0.3173850 \cdot 10^{2}$	$-0.1841757 \cdot 10^{2}$
A_1	$+0.1143818 \cdot 10^{2}$	$+0.5282950 \cdot 10^{0}$
A_2	$-0.3833998 \cdot 10^{1}$	$-0.2200477 \cdot 10^{0}$
A_3	$+0.7046692 \cdot 10^{0}$	$+0.9750192 \cdot 10^{-1}$
A_4	$-0.7431486 \cdot 10^{-1}$	$-0.1749183 \cdot 10^{-1}$
A_5	$+0.4153749 \cdot 10^{-2}$	$+0.4954298 \cdot 10^{-3}$
A_6	$-0.9486967 \cdot 10^{-4}$	$+0.2174910 \cdot 10^{-3}$
A_7	–	$-0.2530205 \cdot 10^{-4}$
A_8	–	$+0.8230751 \cdot 10^{-6}$

Table I: Coefficients A_i for series expansion of rate coefficients of impact ionization $< \sigma v >$ and charge exchange ξ_{Ex}

Vacuum threshold condition	Setting of variables
$\rho/B^2 < \rho_{min}/B^2_{vac}$	$T_e \leftarrow T_0$ $T_i \leftarrow T_0$ $\overline{v}_i \leftarrow \overline{v}_0$ $\overline{B} \leftarrow \overline{B}_{vac}(I_{r,z})$
$\rho_0 < \rho_{0\,min}$	$T_0 \leftarrow T_i$ $\overline{v}_0 \leftarrow \overline{v}_i$
$\rho/B^2 < \rho_{min}/B^2_{vac}$ and $\rho_0 < \rho_{0\,min}$	$T_e \leftarrow 2\text{eV}$ $T_i \leftarrow 2\text{eV}$ $T_0 \leftarrow 2\text{eV}$ $\overline{v}_i \leftarrow \overline{v}_i(\frac{\rho}{\rho_{min}})$ $\overline{v}_0 \leftarrow \overline{v}_0(\frac{\rho_0}{\rho_{0\,min}})$ $\overline{B} \leftarrow \overline{B}_{vac}(I_{r,z})$

Table II: Variables and settings below the thresholds for the vacuum computation and the end of the neutral density computation

Experiment simulation		*a*	*b*	*c*	*d*	
Energy of power source	W_0	30	120	250	280	kJ
Load voltage	U_0	160	240	20	60	kV
Capacity of power source	C_0	1.56	4.2	1.25	156	μF
External inductance	$L_0 + L_c$	45	20	13.5	7	nH
Current rise time	$\tau_0/4$	400	480	6.5	1.6	μs
Filling pressure D_2	p_0	$2.5 - 5$	$4 - 6$	≈ 2	$2 - 4$	mbar
Length of inner electrode	l_{ie}	60	70	350	410	mm
Radius of inner electrode	r_{ie}	25	45	185	66.5	mm
Radius of outer electrode	r_{oe}	68	100	232	95	mm
Length of insulator	l_{is}	36	40	100	100	mm

Table III: Experimental parameters used in the computations for the experiments *a*: SPEED1/15/, *b*: SPEED2/30/, *c*: Frascati 1 MJ operated at 250 kJ/2,3/, *d*: POSEIDON/16/

Figure Captions

Fig. 1: Contour line diagrams at three time steps (from top to bottom: 50, 100, 130 ns) of a fine-mesh ignition calculation for SPEED 1, from left to right: plasma density, neutral density, electron temperature

Fig. 2: Temporal profiles at a point near the insulator (fine-mesh ignition calculation for SPEED 1)

Fig. 3: Contour line diagrams from SPEED 1 calculations at 250 ns, top: neutral and plasma densities (three-fluid), bottom: plasma density from a two-fluid calculation

Fig. 4: Frascati 1 MJ plasma focus: calculated temporal profiles of the plasma and neutral density (above); the electron temperature, the total inductance and its time derivative (below) at a fixed observation point close to the insulator

Fig. 5: POSEIDON: calculated temporal profiles of the plasma and neutral density (above) and the electron temperature (below) at a fixed observation point close to the insulator (The T_e peaks are due to numerical fluctuations near the threshold between the vacuum and finite-density solutions.)

Fig. 6: Contour lines from a POSEIDON calculation at 400 ns, from top to bottom: plasma density, neutral density, electron temperature, vector diagram of current density, contour diagram of current density

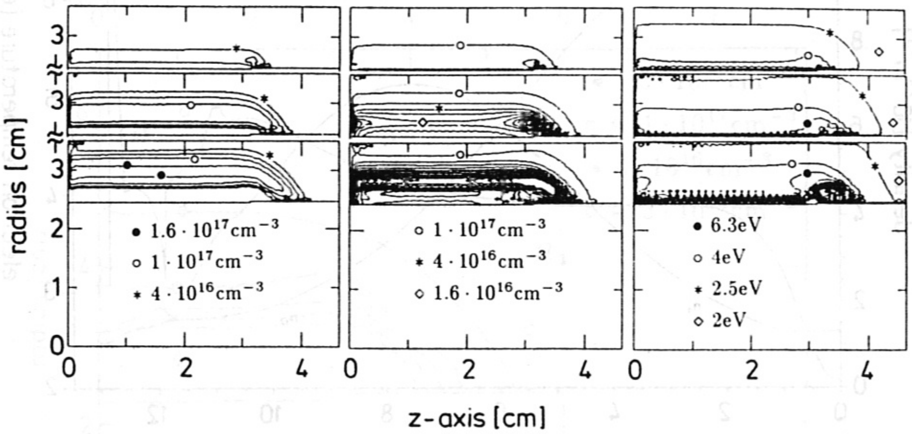

Fig. 1: Contour line diagrams at three time steps (from top to bottom: 50, 100, 130 ns) of a fine-mesh ignition calculation for SPEED 1, from left to right: plasma density, neutral density, electron temperature

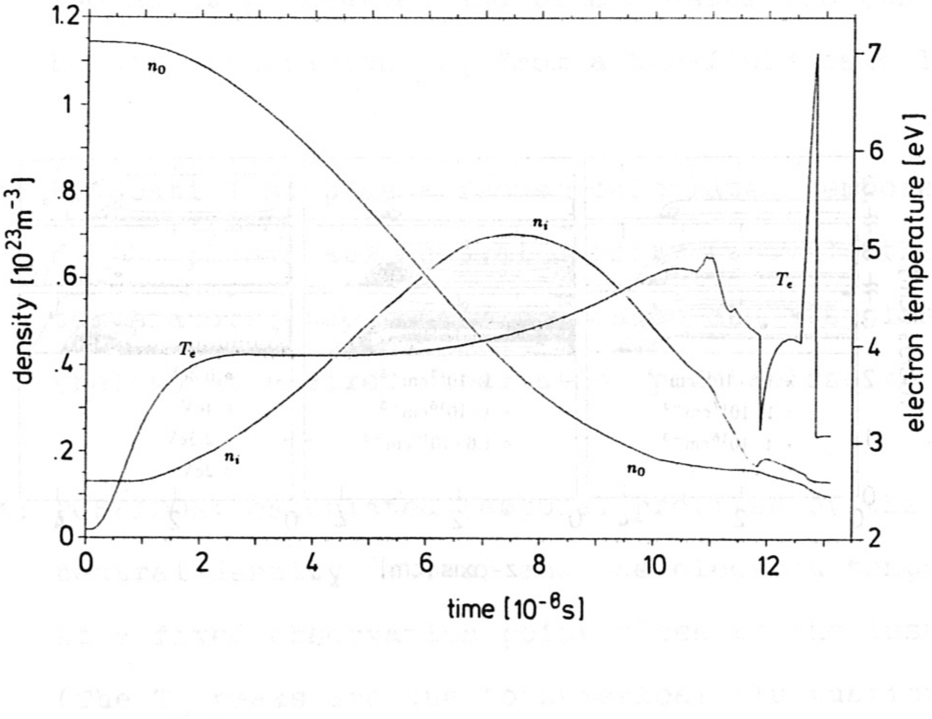

Fig. 2: Temporal profiles at a point near the insulator (fine-mesh ignition calculation for SPEED 1)

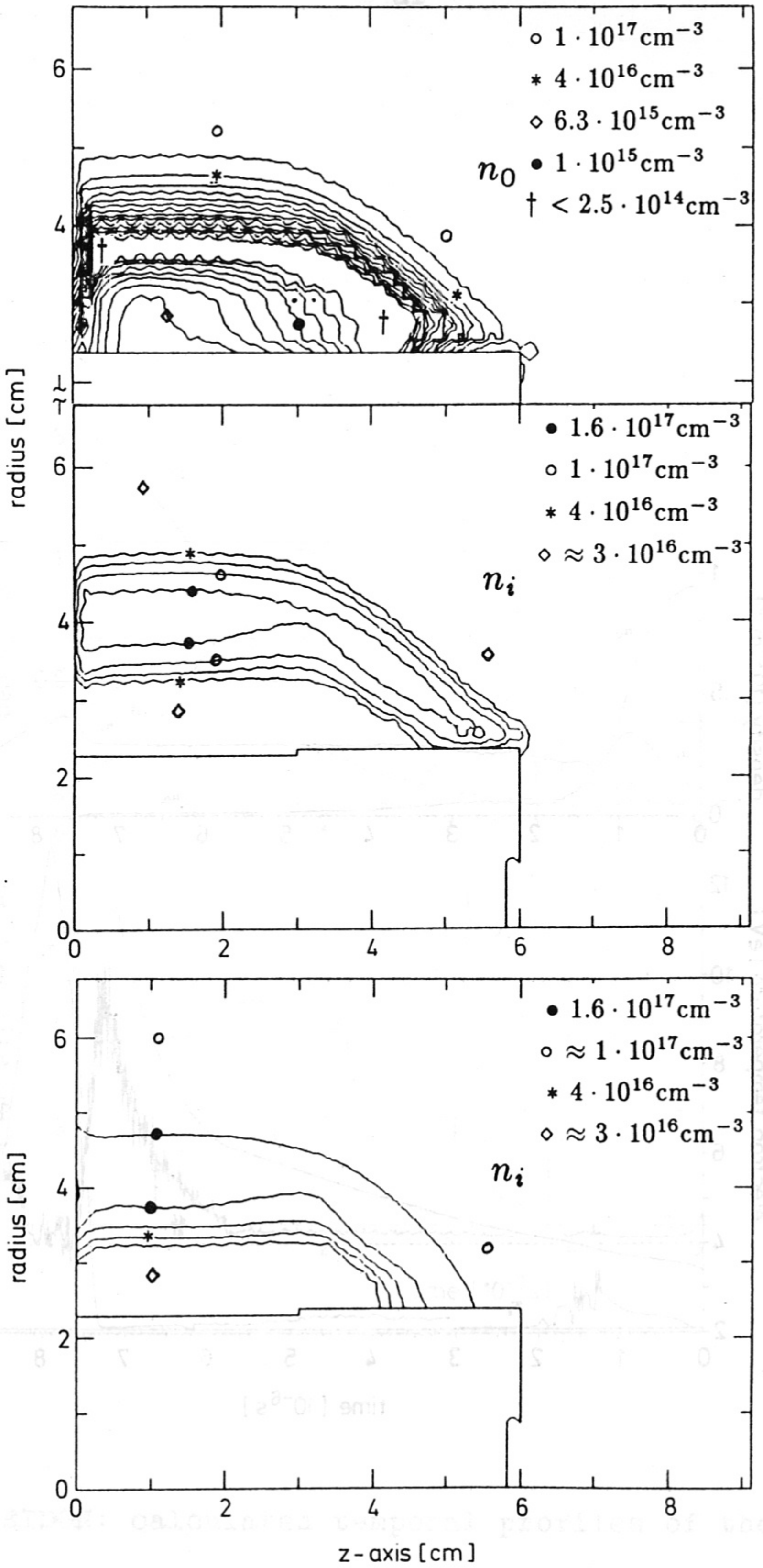

Fig. 3: Contour line diagrams from SPEED 1 calculations at 250 ns, top: neutral and plasma densities (three-fluid), bottom: plasma density from a two-fluid calculation

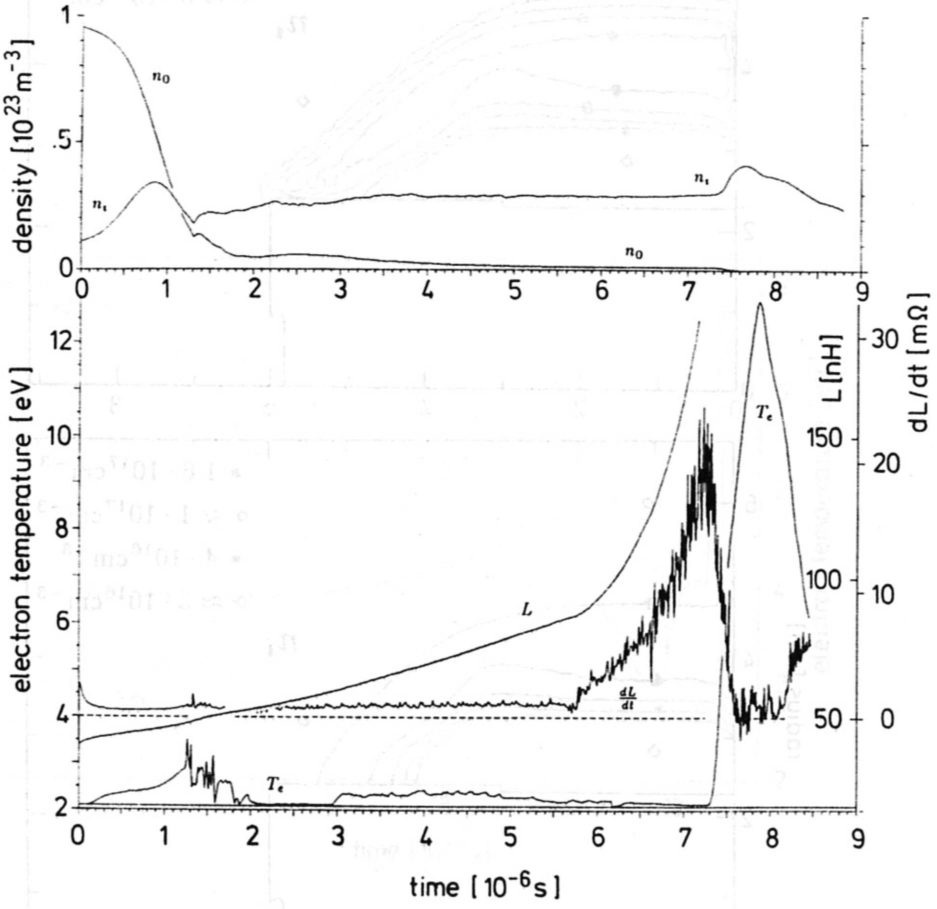

Fig. 4: Frascati 1 MJ plasma focus: calculated temporal profiles of the plasma and neutral density (above); the electron temperature, the total inductance and its time derivative (below) at a fixed observation point close to the insulator

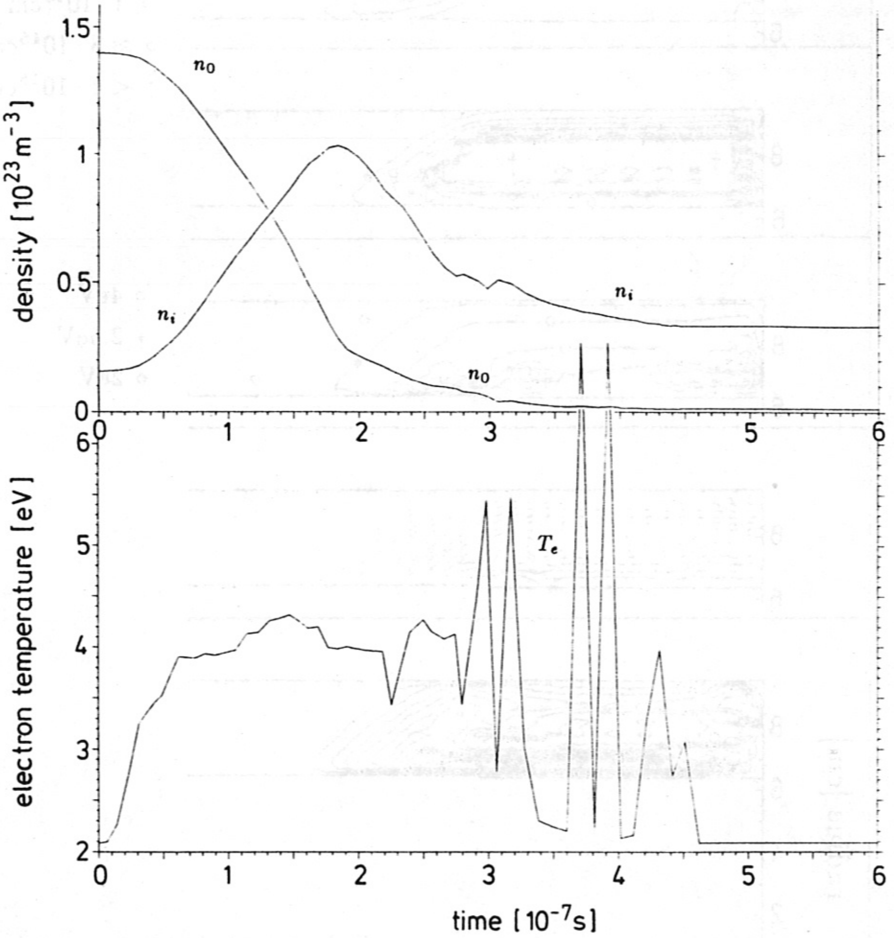

Fig. 5: POSEIDON: calculated temporal profiles of the plasma and neutral density (above) and the electron temperature (below) at a fixed observation point close to the insulator (The T_e peaks are due to numerical fluctuations near the threshold between the vacuum and finite-density solutions.)

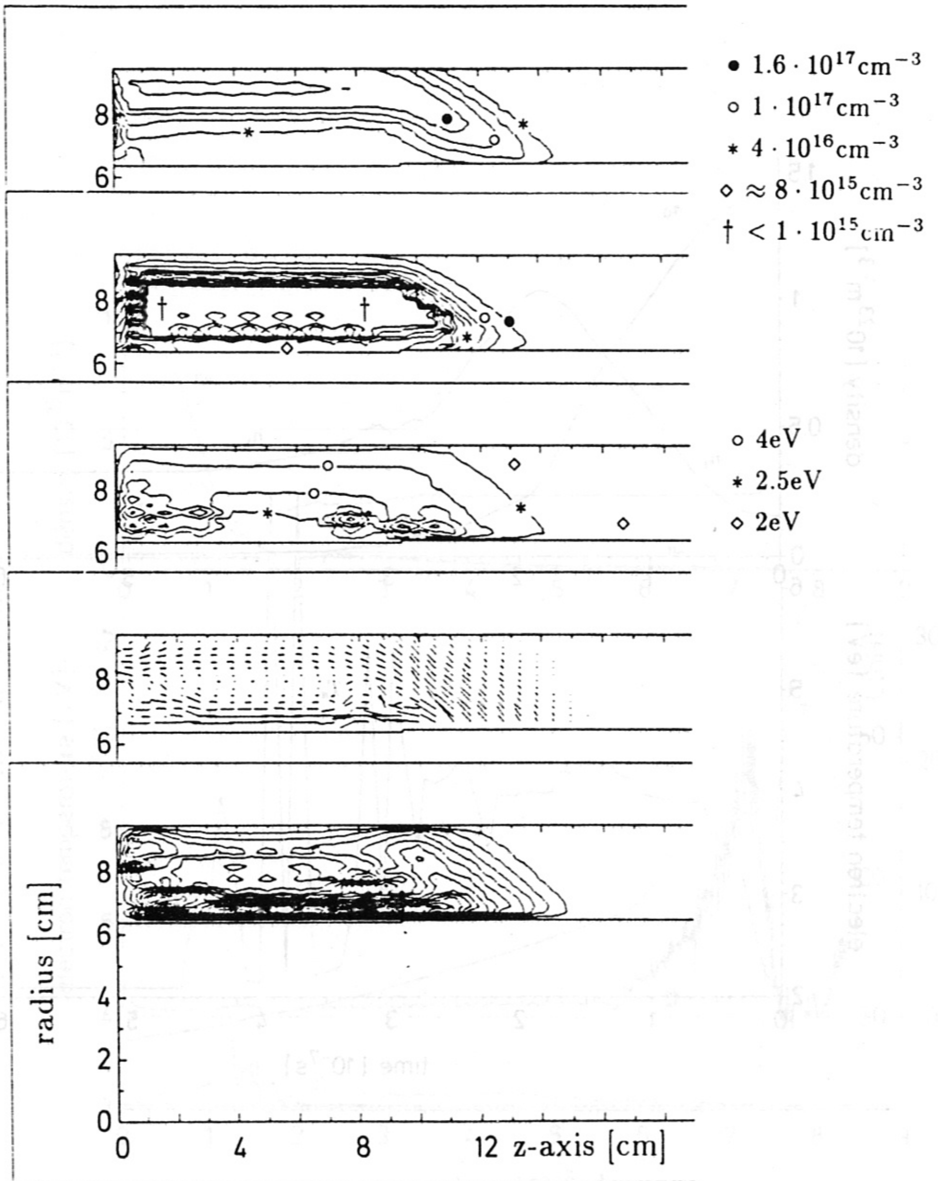

Fig. 6: Contour lines from a POSEIDON calculation at 400 ns, from top to bottom: plasma density, neutral density, electron temperature, vector diagram of current density, contour diagram of current density